

# Unveiling the emergent traits of chiral spin textures in magnetic multilayers

Xiaoye Chen,<sup>1,2</sup> Ming Lin,<sup>1,\*</sup> Jian Feng Kong,<sup>3,\*</sup> Hui Ru Tan,<sup>1</sup> Anthony K.C. Tan,<sup>2</sup> Soong-Geun Je,<sup>4</sup>  
Hang Khume Tan,<sup>1,2</sup> Khoong Hong Khoo,<sup>3</sup> Mi-Young Im,<sup>4</sup> and Anjan Soumyanarayanan<sup>1,2,5,†</sup>

<sup>1</sup>*Institute of Materials Research & Engineering, Agency for Science,  
Technology & Research (A\*STAR), 138634 Singapore*

<sup>2</sup>*Data Storage Institute, Agency for Science, Technology & Research (A\*STAR), 138634 Singapore*

<sup>3</sup>*Institute of High Performance Computing, Agency for Science,  
Technology & Research (A\*STAR), 138632 Singapore*

<sup>4</sup>*Center for X-ray Optics, Lawrence Berkeley National Laboratory, Berkeley, California 94720, USA*

<sup>5</sup>*Physics Department, National University of Singapore (NUS), 117551 Singapore*

Magnetic skyrmions are topologically wound nanoscale textures of spins whose ambient stability and electrical manipulation in multilayer films have led to an explosion of research activities. While past efforts focused predominantly on isolated skyrmions, recently ensembles of chiral spin textures, consisting of skyrmions and magnetic stripes, were shown to possess rich interactions with potential for device applications. However, several fundamental aspects of chiral spin texture phenomenology remain to be elucidated, including their domain wall structure, thermodynamic stability, and morphological transitions. Here we unveil the evolution of these textural characteristics on a tunable multilayer platform – wherein chiral interactions governing spin texture energetics can be widely varied – using a combination of full-field electron and soft X-ray microscopies with numerical simulations. With increasing chiral interactions, we demonstrate the emergence of Néel helicity, followed by a marked reduction in domain compressibility, and finally a transformation in the skyrmion formation mechanism. Together with an analytical model, these experiments establish a comprehensive microscopic framework for investigating and tailoring chiral spin texture character in multilayer films.

## Introduction

Seminal advances in tailoring interfacial interactions in magnetic thin films have led to the room temperature (RT) stabilization of nanoscale spin textures – most notably magnetic skyrmions<sup>1–4</sup>. In light of past efforts on magnetic bubbles and domain walls (DWs)<sup>5,6</sup>, the excitement around magnetic skyrmions stems largely from their non-trivial topology, small size, and their coupling to electrical stimuli. Firstly, skyrmions possess finite topological charge, which emerges from the material-specific handedness and manifests as the chirality of spins winding around their centre<sup>7</sup>. The unique spin structure of skyrmions facilitates their electrical detection<sup>7,8</sup>, while also enabling them to remain stable at sizes down to 2 nm<sup>9,10</sup>. Importantly, they can be electrically generated,<sup>11–14</sup> and driven at relatively high efficiency using electrical currents<sup>2,15</sup>.

While such sparse, isolated skyrmions in chiral multilayers are attractive for spintronic device applications, equally ripe for exploitation are denser *ensembles of chiral spin textures*, consisting of magnetic stripes and skyrmions. Several recent proposals look to harness these so-called “skyrmion fabrics”<sup>16,17</sup> for reservoir computing. However, a comprehensive microscopic picture of chiral spin texture phenomenology, and their response to external stimuli, remains to be established. While some reports confirm their Néel helicity in chiral multilayers<sup>3,18</sup>, others have reported a considerable Bloch component with a layer- and material-dependent magnitude<sup>19,20</sup>. Meanwhile, experimental investigations of the field evolution of their size have focused narrowly on “bubble skyrmions”<sup>3</sup>. Even theoretical ef-

forts, while fully exploring isolated skyrmions, are yet to examine the rich interactions between skyrmions and stripes<sup>21,22</sup>. Finally, while morphological transitions from stripes to skyrmions have been demonstrated<sup>14,23</sup>, the thermodynamic mechanism of skyrmion formation is not understood. Elucidating the microscopic origin of these attributes necessitates a multi-modal investigation of chiral spin textures with varying magnetic interactions on a single material platform.

Much of the character of chiral spin textures can be tuned by a single material parameter,  $\kappa = \pi D/4\sqrt{AK_{\text{eff}}}$ , where  $D$  is the interfacial Dzyaloshinskii-Moriya interaction (iDMI),  $A$  is the exchange stiffness and  $K_{\text{eff}}$  is the effective uniaxial anisotropy<sup>24–26</sup>. Within a simple analytical model without assumption of sample symmetry,  $\kappa$  is associated with the DW energy —  $\kappa > 1$  implies that DW energy density is negative<sup>24,27</sup>. Here, we investigate the emergent characteristics of chiral spin textures over a wide range of  $\kappa$  on a tunable Co/Pt-based multilayer platform. Exploiting the complementary sensitivity of Lorentz transmission electron microscopy (LTEM) and magnetic transmission soft X-ray microscopy (MTXM), to textural characteristics, we elucidate the evolution of DW helicity, domain compressibility, and skyrmion formation mechanism with increasing  $\kappa$ . In conjunction with micromagnetic simulations and an analytical model, we establish a microscopic framework for spin texture character in multilayer films.

Our work is performed at RT using Co/Pt-based multilayer stacks with out-of-plane (OP) anisotropy, which are established hosts of magnetic textures<sup>28</sup>. While

symmetric stacks have negligible total iDMI, asymmetric stacks, such as (Ir or Ta)/Co/Pt can have sizable iDMI ( $D > 1 \text{ mJ/m}^2$ ) – relevant to chiral magnetic textures<sup>1–3</sup>. The inclusion of Fe – as in Ir/Fe/Co/Pt stacks – enhances the iDMI, while  $D$  and  $K_{\text{eff}}$  can be smoothly modulated by Fe and Co thicknesses<sup>4</sup>. Here we study four samples each comprising 1 nm thick FM layers – identified by their  $\text{Fe}(\mathbf{x})/\text{Co}(\mathbf{y})$  composition (Table I) – wherein the active stack is repeated 14 times to optimize full-field magnetic contrast. Interfacial interactions are progressively introduced and quantified using established techniques<sup>1,2,4</sup>, with the estimated iDMI ( $D_{\text{est}}$ ) varying over 0 – 2  $\text{mJ/m}^2$  and  $K_{\text{eff}}$  over 0.08 – 0.70  $\text{MJ/m}^3$  (Experimental Section, SM1). Notably, the  $D_{\text{est}}$  determined for the 14-stack multilayers studied here are in line with measured values on corresponding single stacks from Brillouin light scattering (BLS) experiments<sup>29</sup>. Consequently,  $\kappa$  varies over 0 – 1.5, and provides the requisite range for mapping magnetic texture evolution.

### DW Helicity

The introduction of iDMI should lead to a measurable change in DW helicity of skyrmion textures<sup>7,30</sup>. LTEM imaging – wherein magnetic contrast results from the magnetization curl parallel to the electron beam – is particularly sensitive to such changes. For normal beam incidence (zero tilt), a pair of homochiral Bloch DWs should express symmetric contrast about their center, while Néel DWs should exhibit no contrast as their curl is perpendicular to the beam<sup>31</sup>. Meanwhile, the positions of Néel DWs can be deduced by tilting the sample (Figure 1a), whereupon antisymmetric domain contrast can be observed<sup>18</sup>. To visualize this evolution, we perform tilt-dependent LTEM imaging with samples deposited on  $\text{SiO}_x$  membranes (see Experimental Section). For ease of analysis, we use OP magnetic fields ( $\mu_0 H$ ) large enough to ensure adjacency of pairs of DWs (i.e. thin domains). Artifacts due to granularity and membrane waviness are mitigated using a recipe that extracts  $\sim 1000$  linecuts across domains imaged over a  $5 \mu\text{m}$  field-of-view (see SM2).

Figure 1 shows stark differences in tilt-dependent LTEM

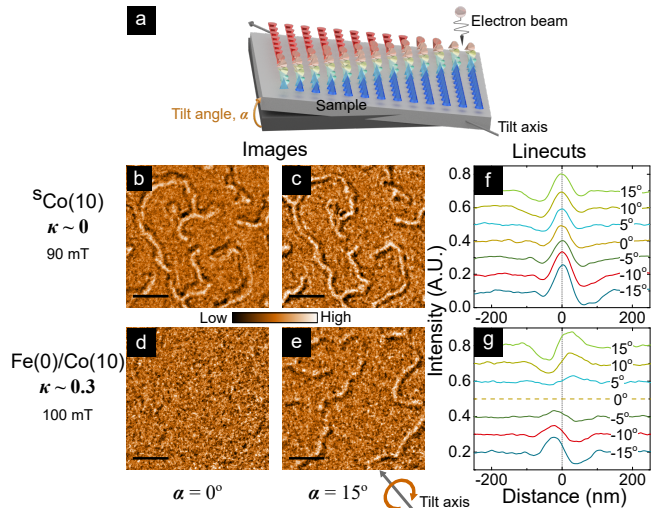


**Figure 1. DW Helicity from Tilt-Dependent LTEM Imaging.** (a) Schematic diagram of LTEM imaging geometry with sample (illustrated here with a Néel DW) tilted at angle  $\alpha$  with respect to the plane normal to the electron beam. The tilt axis is shown below (e). (b–e) Representative LTEM images (scale bar:  $0.5 \mu\text{m}$ ) acquired on samples  $^{\text{S}}\text{Co}(10)$  (b–c) and  $\text{Fe}(0)/\text{Co}(10)$  (d–e) at  $\mu_0 H = 90$  and  $100 \text{ mT}$  respectively for  $\alpha = 0^\circ$  (b,d) and  $\alpha = 15^\circ$  (c,e), with  $-2 \text{ mm}$  defocus. (f–g) Average cross-sectional linecuts across domains detected in LTEM images of  $^{\text{S}}\text{Co}(10)$  (f) and  $\text{Fe}(0)/\text{Co}(10)$  (g), with  $\alpha$  varied over  $\pm 15^\circ$ . Each curve represents the average of  $\sim 1,000$  linecuts extracted from domains imaged over a  $5 \mu\text{m}$  field-of-view using an automated recipe. Dashed vertical lines mark the domain center.

Acronym	Stack Composition ( $\text{\AA}$ )	$K_{\text{eff}}$	$D_{\text{est}}$	$\kappa$
$^{\text{S}}\text{Co}(10)$	[Pt(10)/Co(10)/Pt(10)] <sub>14</sub>	0.68	0	0
$\text{Fe}(0)/\text{Co}(10)$	[Ir(10)/Co(10)/Pt(10)] <sub>14</sub>	0.47	1.3	0.3
$\text{Fe}(2)/\text{Co}(8)$	[Ir(10)/Fe(2)/Co(8)/Pt(10)] <sub>14</sub>	0.22	1.8	0.9
$\text{Fe}(3)/\text{Co}(7)$	[Ir(10)/Fe(3)/Co(7)/Pt(10)] <sub>14</sub>	0.08	2.0	1.5

**Table I. Sample Compositions.** List of multilayer samples used in this work, with layer thickness in angstroms in parentheses (see Experimental Section, SM1 for full-stack details). Corresponding magnetic properties are listed: effective anisotropy  $K_{\text{eff}}$  ( $\text{MJ/m}^3$ ), estimated iDMI  $D_{\text{est}}$  ( $\text{mJ/m}^2$ ) and the stability parameter,  $\kappa$ . The samples are henceforth referred to by their **acronym**.

results for  $^{\text{S}}\text{Co}(10)$  and  $\text{Fe}(0)/\text{Co}(10)$ . First,  $^{\text{S}}\text{Co}(10)$  ( $D_{\text{est}} \simeq 0$ ,  $\kappa \simeq 0$ ) shows strong, symmetric contrast about the domain center at zero tilt (Figure 1b), with a small antisymmetric component at finite tilt angle (Figure 1c,f). This is consistent with Bloch DWs expected for symmetric stacks<sup>32–34</sup>. Micromagnetic simulations performed with  $^{\text{S}}\text{Co}(10)$  parameters (see Experimental Section) suggest that the Bloch DWs are achiral, i.e. lack fixed handedness (see SM4). In comparison,  $\text{Fe}(0)/\text{Co}(10)$  ( $D_{\text{est}} \simeq 1.3 \text{ mJ/m}^2$ ,  $\kappa \simeq 0.3$ ) shows no contrast at zero tilt (Figure 1d). Contrast at finite tilt is consistently antisymmetric – and whose amplitude increases with tilt angle (Figure 1e,g) – consistent with Néel DWs. The lack of measurable symmetric contrast in Figure 1g suggests that any Bloch component – e.g. due to layer-dependent chirality<sup>19,20</sup> – is negligibly small<sup>34</sup>. Micromagnetic simulations for  $\text{Fe}(0)/\text{Co}(10)$  also reflect the limited influence of such layer dependent variations, which are further suppressed if moderate interlayer exchange coupling is included (see SM4). Finally, similar experiments on  $\kappa \gtrsim 1$  samples produce results fully consistent with  $\text{Fe}(0)/\text{Co}(10)$  (see SM3). These results indicate that chiral interactions in the  $\kappa \sim 0.3$  sample are sufficiently large to transform achiral Bloch textures ( $\kappa \simeq 0$ ) to homochiral Néel textures<sup>27</sup>.

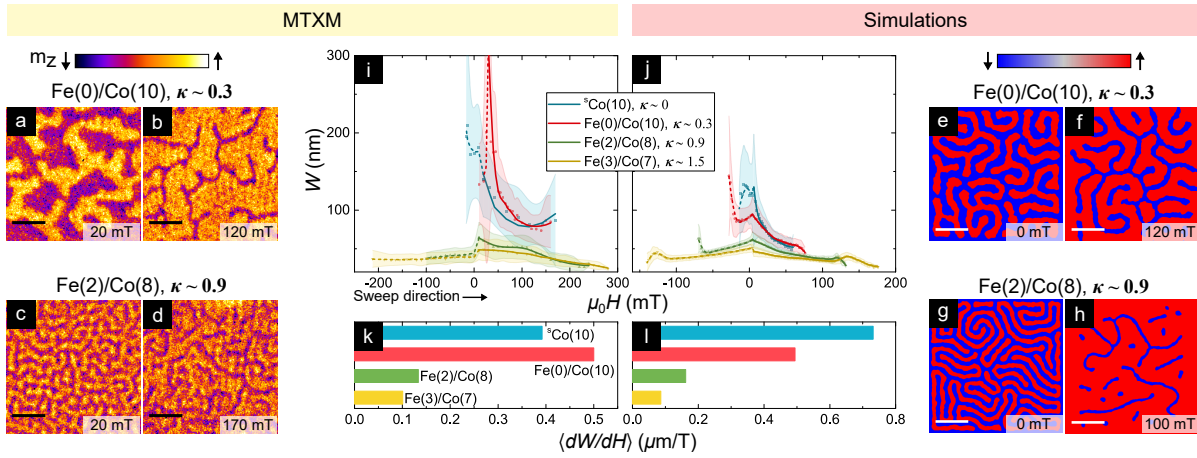


Figure 2. **Domain Width Field Evolution: MTXM Imaging and Simulations.** (a-d) MTXM images of samples Fe(0)/Co(10) ( $\kappa \sim 0.3$ : a-b) and Fe(2)/Co(8) ( $\kappa \sim 0.9$ , c-d) – showing domain evolution from near-zero (a,c) to near-saturation (b,d) fields. (scalebar:  $0.5 \mu\text{m}$ ) (e-h) Simulated magnetization images for magnetic parameters consistent with Fe(0)/Co(10) (e-f) and Fe(2)/Co(8) (g-h) – showing the corresponding evolution from zero (e,g) to higher fields (f,h). (i-j) Average minority polarisation domain width,  $W(H)$ , with varying magnetic field from MTXM experiments (i) and simulations (j) on all four samples studied in this work. Each  $W(H)$  data point is a full field-of-view mean (shaded band is the standard deviation) determined using an automated recipe (see SM2). Solid and dashed lines, guides to the eye, represent magnetization in the negative and positive vertical direction respectively. (k-l) Average magnitude of compressibility,  $\langle dW/dH \rangle$ , for the four samples from experiments (k) and simulations (l), corresponding to the average gradients in (i) and (j) respectively for  $\mu_0 H > 0$ .

### Domain Compressibility

Having established DW helicity evolution, we turn to domain characteristics – which evolve with OP field in addition to magnetic interactions<sup>1,2,4</sup>. Both stripes and skyrmions can be collectively characterized by a single length scale,  $W$ , defined as domain width of stripes and diameter of skyrmions of the minority polarisation. Notably, the field-induced variation of  $W$ , or  $dW/dH$  – termed as **domain compressibility**<sup>35</sup> – should also evolve with  $\kappa$ <sup>4,25,36</sup>. MTXM imaging – wherein magnetic circular dichroic contrast is proportional to local OP magnetization<sup>37</sup> – is well-suited to measure  $W$ . Therefore, we performed MTXM imaging with varying OP field using samples deposited on  $\text{Si}_3\text{N}_4$  membranes, complemented by micromagnetic simulations (see Experimental Section).  $W$  was determined as an averaged quantity over the full field-of-view of about  $5 \mu\text{m}$  using an automated recipe to mitigate granularity effects (see SM2). The identity of the minority polarisation flips at the coercive field, resulting in a sharp kink in  $W$ .

Figure 2 shows MTXM (a-d,i,k) and simulation results (e-h,j,l) of  $W(H)$  across samples with varying  $\kappa$ . On one hand, for  $\kappa \ll 1$  – illustrated for Fe(0)/Co(10) ( $\kappa \sim 0.3$ , Figure 2a-b,i) –  $W$  shrinks rapidly with field ( $\langle dW/dH \rangle \sim 0.5 \mu\text{m}/\text{T}$ , Figure 2k). Such **highly compressible behavior** is well reproduced by simulations (Figure 2e-f). One difference from experi-

ments is the relative order of  $\langle dW/dH \rangle$  for  $^{\text{S}}\text{Co}(10)$  and Fe(0)/Co(10). The likely source of this discrepancy is the domain nucleation field, which affects domain compressibility. In low  $\kappa$  samples such as  $^{\text{S}}\text{Co}(10)$  and Fe(0)/Co(10), domain nucleation may be dominated by extrinsic factors such as grains<sup>38</sup> that are not accounted for in our simulations. Nevertheless, the  $W(H)$  trend of chiral Néel textures (Fe(0)/Co(10)) is remarkably similar to achiral Bloch textures ( $^{\text{S}}\text{Co}(10)$ )<sup>39</sup>, Figure 2i-j). This suggests that domain compressibility is largely independent of DW helicity. On the other hand, for  $\kappa \gtrsim 1$  – shown for Fe(2)/Co(8) ( $\kappa \sim 0.9$ , Figure 2c-d,i) – the  $W(H)$  variation is much reduced ( $\langle dW/dH \rangle \sim 0.1 \mu\text{m}/\text{T}$ , Figure 2k)<sup>40</sup>. Similarly rigid or incompressible behavior is seen for Fe(3)/Co(7) ( $\kappa \sim 1.5$ ), albeit at reduced  $W$ , and in the analysis of LTEM images (see SM3). Finally, simulated trends for  $\kappa \gtrsim 1$  are also in line with these results (Figure 2g-h,j,l), suggesting that the contrast may be understood within a micromagnetic energy framework.

To elucidate the compressibility evolution, we use an analytical model of 1D periodic domains within an infinite magnetic slab of thickness  $t$ , domain period  $\lambda$ , and DW width  $\Delta$  (Figure 3a). This model is chosen because it considers the interactions between neighbouring stripes, which we believe is essential to the compressibility phenomenon. The total energy density is given by<sup>21</sup>:

$$\varepsilon_{\text{tot}} = \frac{2}{\lambda} \left[ \frac{2A}{\Delta} + 2K_u \Delta + \pi D \sin \psi \right] + \varepsilon_{d,s} + \varepsilon_{d,v} - M_s \left( 1 - \frac{2W}{\lambda} \right) B_z, \quad (1)$$



where the magnetostatic energy densities due to surface ( $\varepsilon_{d,s}$ ) and volume charges ( $\varepsilon_{d,v}$ ) are:

$$\varepsilon_{d,s} = \frac{\mu_0 M_s^2}{2} \left(1 - \frac{2W}{\lambda}\right)^2 + \frac{2\pi\mu_0 M_s^2 \Delta^2}{\lambda t} \sum_{n=1}^{\infty} \frac{\sin^2 \frac{\pi n W}{\lambda}}{\sinh^2 \frac{\pi^2 n \Delta}{\lambda}} \frac{1 - \exp\left(-\frac{2\pi n t}{\lambda}\right)}{n}, \text{ and} \quad (2)$$

$$\varepsilon_{d,v} = \frac{2\pi\mu_0 M_s^2 \Delta^2 \sin^2 \psi}{\lambda t} \sum_{n=1}^{\infty} \frac{\sin^2 \frac{\pi n W}{\lambda}}{\cosh^2 \frac{\pi^2 n \Delta}{\lambda}} \frac{\exp\left(-\frac{2\pi n t}{\lambda}\right) + \frac{2\pi n t}{\lambda} - 1}{n}. \quad (3)$$

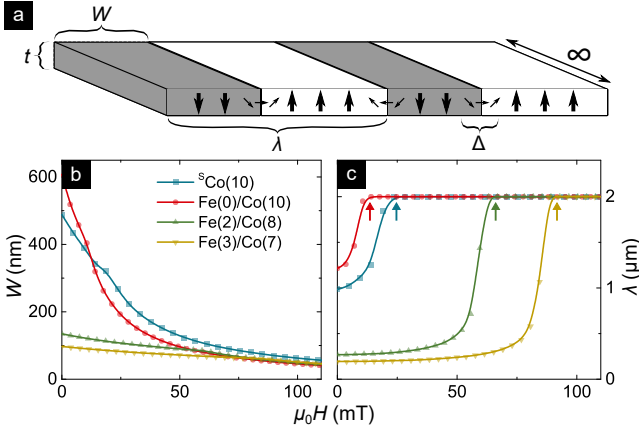


Figure 3. **1D Model for Domain Compressibility Evolution.** (a) Schematic of the simplified analytical model of 1D periodic domains used to interpret the observed domain compressibility. Minority domains of DW width  $\Delta$ , total width  $W$ , and period  $\lambda$  are considered within an infinitely long magnetic slab of thickness  $t$  and breadth  $2 \mu\text{m}$ . (b-c) Field evolution of domain width,  $W(H)$  (b, c.f. Figure 2i-j) and period,  $\lambda(H)$  (c), obtained from the 1D model (details in text) for magnetic parameters consistent with the samples of interest. Arrows in (c) mark the saturation field,  $H_S$ , predicted by the model.

The field evolutions of  $W$  and  $\lambda$  (Figure 3b-c) are obtained by numerically minimizing  $\varepsilon_{\text{tot}}$  with respect to  $\lambda$ ,  $W$ , and  $\Delta$ . Notably, the 1D model reproduces  $\kappa$  dependence of compressibility found in experiments (Figure 2i) and simulations (Figure 2j): domains are highly compressible for  $\kappa \ll 1$ , and relatively incompressible for  $\kappa \gtrsim 1$ . Furthermore, it offers a physical explanation for the compressibility evolution when viewed in conjunction with  $\lambda(H)$ . The latter is indicative of the saturation field,  $H_S$  (arrows in Figure 3c), and the domain density. For  $\kappa \gtrsim 1$ , wherein  $H_S$  is higher (see SM1), domain nucleation occurs just below  $H_S$  with smaller size (Figure 3b) and very close proximity (Figure 3c). The latter ensures *mutual confinement* of domains, limiting the expansion of  $W$  with reducing  $H$ . Therefore, as  $H$  is increased from zero,  $\kappa \gtrsim 1$  domains have limited latitude for compression, and  $W(H)$  is nearly constant – expectedly near the lower cut-off ( $W \sim \Delta$ ). The converse argument holds for  $\kappa \ll 1$  domains, which explains their highly compressible  $W(H)$  behavior.

The marked variation of domain compressibility with

$\kappa$ , its direct experimental accessibility, and consistency with grain-free simulations and the 1D model, establish compressibility as an important classifier of skyrmions (and stripes). Compressibility incorporates energetic considerations underlying a theoretically proposed “minimum skyrmion size” metric for isolated skyrmions<sup>21</sup> (details in SM6), while also being relatively robust to material complexities such as grains and defects compared to the size of isolated skyrmions<sup>21,41</sup>. Therefore, it can serve as a useful means to experimentally differentiate highly compressible “bubble” skyrmions from relatively incompressible “compact” skyrmions. Meanwhile, the remarkable difference in compressibility between samples with  $\kappa \ll 1$  and  $\kappa \gtrsim 1$  demonstrates the importance of considering interactions between skyrmion textures within theoretical models. Further, it hints at the possibility of using effective fields, generated by material, geometric, or external means<sup>36,42,43</sup>, to tune the size and morphology of stabilized spin textures.

### Skyrmion Formation Mechanism

While skyrmions are known to emerge from stripes with increasing field, the transition may involve one or more mechanisms or paths. Notably,  $\kappa$ , which determines DW stability, is also expected to affect this stripe-to-skyrmion transition. First, we visually examine the  $\kappa$ -variation of this transition by tracking the simulated field evolution of a prototypical magnetic stripe (details in SM4). We see for  $\kappa \sim 0.9$  (Figure 4a) that the stripe shrinks smoothly with field, and eventually turns into a single skyrmion. Meanwhile, for  $\kappa \sim 1.5$  (Figure 4b), the stripe abruptly fissions into 4 distinct skyrmions at a characteristic field<sup>44</sup>. These two mechanisms should result in contrasting textural field evolutions that should be detectable in our experiments. Therefore, we statistically examine the field evolution of stripes and skyrmions - distinguished in images by their circularity (see SM2). Here, we choose LTEM imaging, as it enables a clearer distinction between skyrmions and stripes (see SM2).

Figure 4c-f present the field evolution of densities of skyrmions ( $n_S$ ) and stripes ( $n_R$ ) from LTEM and simulations for samples Fe(2)/Co(8) and Fe(3)/Co(7). For each case, highlighted regions at intermediate fields – spanning from  $n_R$  peak to  $n_S$  peak – indicate stripe-



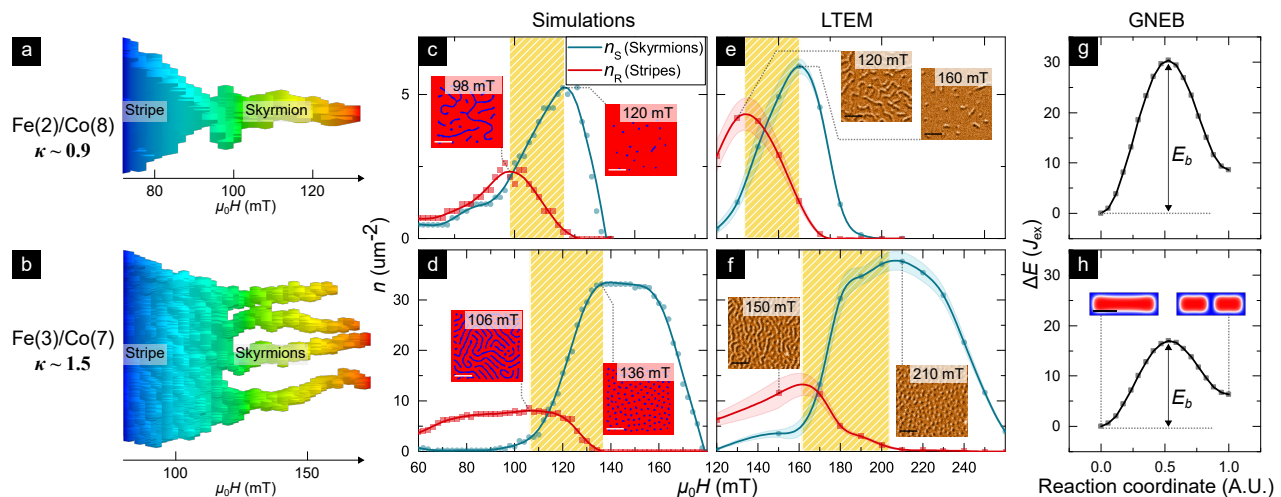


Figure 4. **Evolution of Skyrmion Formation Mechanism.** (a-b) Simulated field evolution of a prototypical stripe after its separation from the labyrinthine state for (a) Fe(2)/Co(8) ( $\kappa \sim 0.9$ ) and (b) Fe(3)/Co(7) ( $\kappa \sim 1.5$ ) parameters. The stripe is identified and isolated in real-space for each field slice and stacked horizontally to form a 3D structure, which is in turn reoriented with the length of the stripe along the vertical and field axis along the horizontal (details in SM4). (c-f) Field evolution of the density of skyrmions ( $n_S$ , teal) and stripes ( $n_R$ , red), as extracted from simulations (c-d) and LTEM imaging (e-f) for samples Fe(2)/Co(8) (c,e) and Fe(3)/Co(7) (d,f) respectively (procedural details in SM2). Highlighted regions denote field ranges corresponding to marked stripe to skyrmion transitions (c.f. a-b). Inset: Simulation and LTEM images immediately before and after stripe-to-skyrmion transitions (scalebar:  $0.5 \mu\text{m}$ ). (g-h) Energy profile (in units of Heisenberg exchange  $J_{\text{ex}}$ ) governing the fission of a stripe for Fe(2)/Co(8) ( $\kappa \sim 0.9$ ) and Fe(3)/Co(7) ( $\kappa \sim 1.5$ ) respectively calculated using GNEB method (details in SM5).  $E_b$  denotes the energy barrier for the fission process, inset of (h) depicts the stripe before and after fission (scalebar:  $0.1 \mu\text{m}$ ).

to-skyrmion transitions, and exhibit contrasting trends. For Fe(2)/Co(8) ( $\kappa \sim 0.9$ , Figure 4c,e) the decrease in  $n_R$  ( $\sim 2-3 \mu\text{m}^{-2}$ ) corresponds to a one-to-one increase in  $n_S$  ( $\sim 2-3 \mu\text{m}^{-2}$ ). This is consistent with the shrinking of one stripe to one skyrmion, thereby resulting in isolated skyrmions (Figure 4c,e: inset). In contrast, for Fe(3)/Co(7) ( $\kappa \sim 1.5$ , Figure 4d,f) the decrease in  $n_R$  ( $\sim 7-8 \mu\text{m}^{-2}$ ) coincides with a four-fold increase in  $n_S$  ( $\sim 30 \mu\text{m}^{-2}$ ). This is in line with the fission of one stripe into  $\sim 4$  skyrmions on average and generates a dense skyrmion lattice (Figure 4d,f: inset)<sup>44</sup>. Thus, we have empirically observed the increased favorability of fission with increasing  $\kappa$  (0.9 to 1.5).

The above observation may be understood from kinetic considerations. The fission of a stripe involves a change in topology and hence should be protected by an energy barrier. To examine the evolution of the barrier height ( $E_b$ ) with  $\kappa$ , we perform geodesic nudged elastic band (GNEB) calculations for Fe(2)/Co(8) and Fe(3)/Co(7) (Figure 4g,h, details in SM5). We found that  $E_b$  for Fe(2)/Co(8) is 40% greater than that for Fe(3)/Co(7). Assuming that entropic effects are comparable across the two compositions<sup>45</sup>, it follows that fission will be greatly suppressed in Fe(2)/Co(8) relative to Fe(3)/Co(7). The suppression of fission in Fe(2)/Co(8) will then require stripes to instead smoothly shrink into skyrmions.

## Outlook

In summary, we have elucidated transitions in three critical characteristics of chiral spin textures. As shown

in Figure 5, these characteristics systematically evolve with  $\kappa$  – the material parameter determining chiral DW stability. First, as  $\kappa$  increases measurably from zero, the DW helicity transitions from achiral Bloch to chiral Néel-type. Next, as  $\kappa$  approaches unity, the domain compressibility is drastically reduced, transforming “bubble” skyrmions into “compact” skyrmions. Finally, for  $\kappa > 1$ , the skyrmion formation mechanism evolves from shrinking to fission of stripes, resulting in the proliferation of compact Néel skyrmions for  $\kappa > 1$ . Our findings – established on a single tunable material platform – provide several valuable insights towards understanding the observed phenomenology of chiral spin textures, notably skyrmions. Firstly, we have shown that a small but finite  $\kappa$  ( $\sim 0.3$ ) enables the formation of Néel DWs with fixed chirality, with no evidence of a Bloch component even for a 14-repeat stack. Next, we have established the compressibility of domains as a robust experimental metric to differentiate bubble and compact skyrmions. Finally, we have shown that the preference for one of two distinct skyrmion formation mechanisms – shrinking and fission – may explain the observation of isolated skyrmions<sup>1,13</sup> in some materials and dense skyrmion lattices<sup>4,9</sup> in others.

These insights provide a timely roadmap to inform stack design for skyrmionic applications – particularly in device architectures that rely on ensembles of chiral spin textures rather than on sparse, isolated skyrmions. For example, selecting a stack with  $0 < \kappa \ll 1$ , hosting highly compressible domains, will enable dynamic tuning of the spin texture morphology with temporal

variation of applied fields. Conversely, if the application requires control of the topology of textures, a  $\kappa \gg 1$  stack, enabling fission-driven skyrmion formation, would be a better fit. Spanning the physics of stripes and skyrmions, our work provides a springboard for their use as “skyrmion fabrics” for applications in unconventional computing<sup>16</sup>.

## Methods

### Sample Fabrication

Multilayer films, comprising Ta(40)/Pt(50)/**[HM(10)/Fe(x)/Co(y)/HM(10)]**14/Pt(20) (HM: heavy metal, number in parentheses indicates thickness in angstroms), were deposited by DC magnetron sputtering at room temperature using a Chiron<sup>TM</sup> UHV system manufactured by Bestec GmbH (base pressure:  $10^{-8}$  Torr). Four samples were studied in this work whose active stack compositions (bolded above) are listed in Table I. To enable direct comparison between different techniques used in this work, the films were simultaneously deposited for magnetometry on thermally oxidized 100 nm Si wafer substrates, for LTEM on 20 nm-thick SiO<sub>2</sub> membrane window grids from SPI Supplies, and for MTXM on 50 – 200 nm thick Si<sub>3</sub>N<sub>4</sub> membranes from Silson. Magnetometry measurements were performed using an EZ11 vibrating sample magnetometer (VSM) made by MicroSense<sup>TM</sup>. The magnetic parameters:  $M_S$ ,  $K_{\text{eff}}$ ,  $A_{\text{est}}$  and  $D_{\text{est}}$  were obtained using protocols consistent with literature<sup>1,2,4,36,46</sup>, and are detailed in SM1.

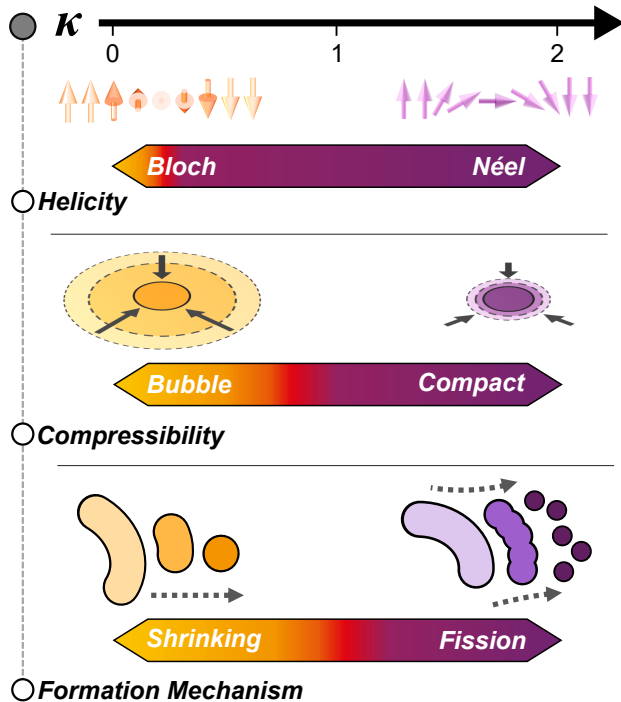


Figure 5.  $\kappa$ -Driven Evolution of Skyrmion Characteristics. Overview of the evolution of multilayer skyrmion characteristics with increasing  $\kappa$  as seen across the samples studied in this work. This includes the change of DW helicity from Bloch to Néel (top), domain compressibility from bubble to compact (middle), and skyrmion formation mechanism from shrinking to fission of stripes (bottom).

### Lorentz TEM Experiments

Lorentz transmission electron microscopy (LTEM) experiments were performed using an FEI Titan S/TEM operated in Lorentz Fresnel mode at 300 kV. A dedicated Lorentz lens for focusing the electron beam was used at a defocus of  $-2$  mm. Meanwhile, the objective lens located at the sample position was switched off for imaging acquisition under field-free conditions, or excited to different strengths to apply out-of-plane magnetic fields ( $-300$  mT to  $+2$  T) for in-situ studies of magnetic texture evolution.

### MTXM Experiments

Full-field MTXM imaging experiments were performed using circularly polarised soft x-rays at the Advanced Light Source (XM-1 BL 6.1.2), using the Co L3 edge ( $\sim 778$  eV) with out-of-plane (OP) sample geometry<sup>37</sup>. OP magnetic fields were applied using an electromagnet, and a pair of horse-shoe poles were used to guide the generated flux.

### Micromagnetic Simulations

Micromagnetic simulations were performed using MuMax3 to interpret the field evolution of the 14 repeat multilayer stacks<sup>47</sup>. The simulation field-of-view used was  $2 \mu\text{m} \times 2 \mu\text{m}$ , and the cell size was kept to  $4 \text{ nm} \times 4 \text{ nm} \times 3 \text{ nm}$ , which is below the exchange length for all samples. The effective medium approximation was used with one layer per stack repetition to account for memory constraints<sup>2</sup>. Hysteresis loops were simulated using protocols described in<sup>47</sup>.

### Image Analysis

Custom-written Python scripts were used for the quantitative analysis of magnetic microscopy images. These scripts comprise routines for image filtering and binarization followed by domain characterization and statistics using standard methods in the scikit-image library<sup>48</sup>. The analysis procedures are detailed in SM2.

We acknowledge the support of the National Supercomputing Centre (NSCC) and A\*STAR Computational Resource Centre (A\*CRC) for computational resources. This work was supported by the SpOT-LITE program (Grant Nos. A1818g0042, A18A6b0057), funded by Singapore’s RIE2020 initiatives, and by the Pharos skyrmion program (Grant No. 1527400026) funded by A\*STAR, Singapore. Works at the ALS were supported by U.S. Department of Energy (DE-AC02-05CH11231). M.-Y. Im acknowledges support by Lawrence Berkeley National Laboratory through the Laboratory Directed Research and Development (LDRD) Program. The authors thank Pin Ho and Ramu Maddu for helpful discussions.

\* These authors contributed equally to this work.

† anjan@imre.a-star.edu.sg

- [1] C. Moreau-Lucaire, C. Moutafis, N. Reyren, J. Sampaio, C. a. F. Vaz, N. V. Horne, K. Bouzehouane, K. Garcia, C. Deranlot, P. Warnicke, P. Wohlhüter, J.-M. George, M. Weigand, J. Raabe, V. Cros, and A. Fert, Additive interfacial chiral interaction in multilayers for stabilization of small individual skyrmions at room temperature, *Nature Nanotechnology* **11**, nmano.2015.313 (2016).

- [2] S. Woo, K. Litzius, B. Krüger, M.-Y. Im, L. Caretta, K. Richter, M. Mann, A. Krone, R. M. Reeve, M. Weigand, P. Agrawal, I. Lemesh, M.-A. Mawass, P. Fischer, M. Kläui, and G. S. D. Beach, Observation of room-temperature magnetic skyrmions and their current-driven dynamics in ultrathin metallic ferromagnets, *Nature Materials* **15**, 501 (2016).
- [3] O. Boulle, J. Vogel, H. Yang, S. Pizzini, D. d. S. Chaves, A. Locatelli, T. O. Mentes, A. Sala, L. D. Buda-Prejbeanu, O. Klein, M. Belmeguenai, Y. Roussigné, A. Stashkevich, S. M. Chérif, L. Aballe, M. Foerster, M. Chshiev, S. Auffret, I. M. Miron, and G. Gaudin, Room-temperature chiral magnetic skyrmions in ultrathin magnetic nanostructures, *Nature Nanotechnology* **11**, 449 (2016).
- [4] A. Soumyanarayanan, M. Raju, A. L. G. Oyarce, A. K. C. Tan, M.-Y. Im, A. P. Petrović, P. Ho, K. H. Khoo, M. Tran, C. K. Gan, F. Ernult, and C. Panagopoulos, Tunable room-temperature magnetic skyrmions in Ir/Fe/Co/Pt multilayers, *Nature Materials* **16**, nmat4934 (2017).
- [5] A. Bobeck, P. Bonyhard, and J. Geusic, Magnetic bubbles—An emerging new memory technology, *Proceedings of the IEEE* **63**, 1176 (1975).
- [6] S. S. P. Parkin, M. Hayashi, and L. Thomas, Magnetic Domain-Wall Racetrack Memory, *Science* **320**, 190 (2008).
- [7] N. Nagaosa and Y. Tokura, Topological properties and dynamics of magnetic skyrmions, *Nature Nanotechnology* **8**, 899 (2013).
- [8] A. Neubauer, C. Pfleiderer, B. Binz, A. Rosch, R. Ritz, P. G. Niklowitz, and P. Böni, Topological Hall Effect in the A Phase of MnSi, *Physical Review Letters* **102**, 186602 (2009).
- [9] N. Romming, C. Hanneken, M. Menzel, J. E. Bickel, B. Wolter, K. v. Bergmann, A. Kubetzka, and R. Wiesendanger, Writing and Deleting Single Magnetic Skyrmions, *Science* **341**, 636 (2013).
- [10] J. Hagemester, N. Romming, K. von Bergmann, E. Y. Vedmedenko, and R. Wiesendanger, Stability of single skyrmionic bits, *Nature Communications* **6**, 8455 (2015).
- [11] W. Jiang, P. Upadhyaya, W. Zhang, G. Yu, M. B. Jungfleisch, F. Y. Fradin, J. E. Pearson, Y. Tserkovnyak, K. L. Wang, O. Heinonen, S. G. E. t. Velthuis, and A. Hoffmann, Blowing magnetic skyrmion bubbles, *Science* **349**, 283 (2015).
- [12] F. Büttner, I. Lemesh, M. Schneider, B. Pfau, C. M. Günther, P. Hessler, J. Geilhufe, L. Caretta, D. Engel, B. Krüger, J. Viehhaus, S. Eisebitt, and G. S. D. Beach, Field-free deterministic ultrafast creation of magnetic skyrmions by spin-orbit torques, *Nature Nanotechnology* **12**, 1040 (2017).
- [13] S. Woo, K. M. Song, X. Zhang, M. Ezawa, Y. Zhou, X. Liu, M. Weigand, S. Finizio, J. Raabe, M.-C. Park, K.-Y. Lee, J. W. Choi, B.-C. Min, H. C. Koo, and J. Chang, Deterministic creation and deletion of a single magnetic skyrmion observed by direct time-resolved X-ray microscopy, *Nature Electronics* **1**, 288 (2018).
- [14] S.-G. Je, D. Thian, X. Chen, L. Huang, D.-H. Jung, W. Chao, K.-S. Lee, J.-I. Hong, A. Soumyanarayanan, and M.-Y. Im, Targeted Writing and Deleting of Magnetic Skyrmions in Two-Terminal Nanowire Devices, *Nano Letters* **21**, 1253 (2021).
- [15] C. Reichhardt, D. Ray, and C. O. Reichhardt, Collective Transport Properties of Driven Skyrmions with Random Disorder, *Physical Review Letters* **114**, 217202 (2015).
- [16] D. Prychynenko, M. Sitte, K. Litzius, B. Krüger, G. Bourianoff, M. Kläui, J. Sinova, and K. Everschor-Sitte, Magnetic Skyrmion as a Nonlinear Resistive Element: A Potential Building Block for Reservoir Computing, *Physical Review Applied* **9**, 014034 (2018).
- [17] D. Pinna, G. Bourianoff, and K. Everschor-Sitte, Reservoir Computing with Random Skyrmion Textures, *Physical Review Applied* **14**, 054020 (2020).
- [18] S. McVitie, S. Hughes, K. Fallon, S. McFadzean, D. McGrouther, M. Krajinak, W. Legrand, D. Maccariello, S. Collin, K. Garcia, N. Reyren, V. Cros, A. Fert, K. Zeissler, and C. H. Marrows, A transmission electron microscope study of Néel skyrmion magnetic textures in multilayer thin film systems with large interfacial chiral interaction, *Scientific Reports* **8**, 5703 (2018).
- [19] W. Legrand, J.-Y. Chauleau, D. Maccariello, N. Reyren, S. Collin, K. Bouzehouane, N. Jaouen, V. Cros, and A. Fert, Hybrid chiral domain walls and skyrmions in magnetic multilayers, *Science Advances* **4**, eaat0415 (2018).
- [20] Y. Dovzhenko, F. Casola, S. Schlotter, T. X. Zhou, F. Büttner, R. L. Walsworth, G. S. D. Beach, and A. Yacoby, Magnetostatic twists in room-temperature skyrmions explored by nitrogen-vacancy center spin texture reconstruction, *Nature Communications* **9**, 1 (2018).
- [21] F. Büttner, I. Lemesh, and G. S. D. Beach, Theory of isolated magnetic skyrmions: From fundamentals to room temperature applications, *Scientific Reports* **8**, 4464 (2018).
- [22] A. Bernand-Mantel, L. Camosi, A. Wartelle, N. Rougemaille, M. Darques, and L. Ranno, The skyrmion-bubble transition in a ferromagnetic thin film, *SciPost Physics* **4**, 027 (2018).
- [23] I. Lemesh, K. Litzius, M. Böttcher, P. Bassirian, N. Kerber, D. Heinze, J. Zázvorka, F. Büttner, L. Caretta, M. Mann, M. Weigand, S. Finizio, J. Raabe, M.-Y. Im, H. Stoll, G. Schütz, B. Dupé, M. Kläui, and G. S. D. Beach, Current-Induced Skyrmion Generation through Morphological Thermal Transitions in Chiral Ferromagnetic Heterostructures, *Advanced Materials* **30**, 1805461 (2018).
- [24] A. Bogdanov and A. Hubert, Thermodynamically stable magnetic vortex states in magnetic crystals, *Journal of Magnetism and Magnetic Materials* **138**, 255 (1994).
- [25] S. Rohart and A. Thiaville, Skyrmion confinement in ultrathin film nanostructures in the presence of Dzyaloshinskii-Moriya interaction, *Physical Review B* **88**, 184422 (2013).
- [26] A. O. Leonov, T. L. Monchesky, N. Romming, A. Kubetzka, A. N. Bogdanov, and R. Wiesendanger, The properties of isolated chiral skyrmions in thin magnetic films, *New Journal of Physics* **18**, 065003 (2016).
- [27] W. Legrand, N. Ronceray, N. Reyren, D. Maccariello, V. Cros, and A. Fert, Modeling the Shape of Axisymmetric Skyrmions in Magnetic Multilayers, *Physical Review Applied* **10**, 064042 (2018).



- [28] L. Belliard, J. Miltat, V. Kottler, V. Mathet, C. Chappert, and T. Valet, Stripe domains morphology versus layers thickness in CoPt multilayers, *Journal of Applied Physics* **81**, 5315 (1997).
- [29] T. Böttcher, Banibrato Sinha, Burkard Hillebrands, Philipp Pirro, Xiaoye Chen, Hang Khume Tan, Robert Lazkowitzki, Khoong Hong Khoo, and Anjan Soumyanarayanan, Dzyaloshinskii-Moriya Interaction in Ir/Fe/Co/Pt Stacks: A BLS and DFT Study, *Private Communication* **1** (2020).
- [30] F. Hellman, A. Hoffmann, Y. Tserkovnyak, G. S. Beach, E. E. Fullerton, C. Leighton, A. H. MacDonald, D. C. Ralph, D. A. Arena, H. A. Dürr, P. Fischer, J. Grollier, J. P. Heremans, T. Jungwirth, A. V. Kimel, B. Koopmans, I. N. Krivorotov, S. J. May, A. K. Petford-Long, J. M. Rondinelli, N. Samarth, I. K. Schuller, A. N. Slavin, M. D. Stiles, O. Tchernyshyov, A. Thiaville, and B. L. Zink, Interface-induced phenomena in magnetism, *Reviews of Modern Physics* **89**, 025006 (2017).
- [31] M. J. Benitez, A. Hrabec, A. P. Mihai, T. A. Moore, G. Burnell, D. McGrouther, C. H. Marrows, and S. McVitie, Magnetic microscopy and topological stability of homochiral Néel domain walls in a Pt/Co/AlOx trilayer, *Nature Communications* **6**, 8957 (2015).
- [32] J. J. Chess, S. A. Montoya, E. E. Fullerton, and B. J. McMorran, Determination of domain wall chirality using in situ Lorentz transmission electron microscopy, *AIP Advances* **7**, 056807 (2017).
- [33] J. A. Garlow, S. D. Pollard, M. Beleggia, T. Dutta, H. Yang, and Y. Zhu, Quantification of Mixed Bloch-Néel Topological Spin Textures Stabilized by the Dzyaloshinskii-Moriya Interaction in Co/Pd Multilayers, *Physical Review Letters* **122**, 237201 (2019).
- [34] K. Fallon, S. McVitie, W. Legrand, F. Ajejas, D. Maccariello, S. Collin, V. Cros, and N. Reyren, Quantitative imaging of hybrid chiral spin textures in magnetic multilayer systems by Lorentz microscopy, *Physical Review B* **100**, 214431 (2019).
- [35] N. Vernier, J.-P. Adam, S. Eimer, G. Agnus, T. Devolder, T. Hauet, B. Ocker, F. Garcia, and D. Ravelosona, Measurement of magnetization using domain compressibility in CoFeB films with perpendicular anisotropy, *Applied Physics Letters* **104**, 122404 (2014).
- [36] P. Ho, A. K. Tan, S. Goolaup, A. G. Oyarce, M. Raju, L. Huang, A. Soumyanarayanan, and C. Panagopoulos, Geometrically Tailored Skyrmions at Zero Magnetic Field in Multilayered Nanostructures, *Physical Review Applied* **11**, 024064 (2019).
- [37] P. Fischer, M.-Y. Im, C. Baldasseroni, C. Bordel, F. Hellman, J.-S. Lee, and C. S. Fadley, Magnetic imaging with full-field soft X-ray microscopies, *Journal of Electron Spectroscopy and Related Phenomena* **189**, 196 (2013).
- [38] C. P. Quinteros, M. J. C. Burgos, L. J. Albornoz, J. E. Gómez, P. Granell, F. Golmar, M. L. Ibarra, S. Bustingorry, J. Curiale, and M. Granada, Impact of growth conditions on the domain nucleation and domain wall propagation in Pt/Co/Pt stacks, *Journal of Physics D: Applied Physics* **54**, 015002 (2020).
- [39] S. A. Montoya, S. Couture, J. J. Chess, J. C. T. Lee, N. Kent, D. Henze, S. K. Sinha, M.-Y. Im, S. D. Kevan, P. Fischer, B. J. McMorran, V. Lomakin, S. Roy, and E. E. Fullerton, Tailoring magnetic energies to form dipole skyrmions and skyrmion lattices, *Physical Review B* **95**, 024415 (2017).
- [40] N. Romming, A. Kubetzka, C. Hanneken, K. von Bergmann, and R. Wiesendanger, Field-Dependent Size and Shape of Single Magnetic Skyrmions, *Physical Review Letters* **114**, 177203 (2015).
- [41] I. Gross, W. Akhtar, A. Hrabec, J. Sampaio, L. J. Martínez, S. Chouaieb, B. J. Shields, P. Maletinsky, A. Thiaville, S. Rohart, and V. Jacques, Skyrmion morphology in ultrathin magnetic films, *Physical Review Materials* **2**, 024406 (2018).
- [42] G. Chen, A. Mascaraque, A. T. N'Diaye, and A. K. Schmid, Room temperature skyrmion ground state stabilized through interlayer exchange coupling, *Applied Physics Letters* **106**, 242404 (2015).
- [43] W. Legrand, D. Maccariello, F. Ajejas, S. Collin, A. Vecchiola, K. Bouzehouane, N. Reyren, V. Cros, and A. Fert, Room-temperature stabilization of antiferromagnetic skyrmions in synthetic antiferromagnets, *Nature Materials* **19**, 34 (2019).
- [44] A. K. C. Tan, J. Lourembam, X. Chen, P. Ho, H. K. Tan, and A. Soumyanarayanan, Skyrmion generation from irreversible fission of stripes in chiral multilayer films, *Physical Review Materials* **4**, 114419 (2020).
- [45] L. Desplat, D. Suess, J.-V. Kim, and R. L. Stamps, Thermal stability of metastable magnetic skyrmions: Entropic narrowing and significance of internal eigenmodes, *Physical Review B* **98**, 134407 (2018).
- [46] C. Jin, Z.-A. Li, A. Kovács, J. Caron, F. Zheng, F. N. Rybakov, N. S. Kiselev, H. Du, S. Blügel, M. Tian, Y. Zhang, M. Farle, and R. E. Dunin-Borkowski, Control of morphology and formation of highly geometrically confined magnetic skyrmions, *Nature Communications* **8**, 15569 (2017).
- [47] A. Vansteenkiste, J. Leliaert, M. Dvornik, M. Helsen, F. Garcia-Sanchez, and B. Van Waeyenberge, The design and verification of MuMax3, *AIP Advances* **4**, 107133 (2014).
- [48] S. v. d. Walt, J. L. Schönberger, J. Nunez-Iglesias, F. Boulogne, J. D. Warner, N. Yager, E. Gouillart, and T. Yu, scikit-image: image processing in Python, *PeerJ* **2**, e453 (2014).
- [49] S. K. Walton, K. Zeissler, W. R. Branford, and S. Felton, MALTS: A tool to simulate Lorentz Transmission Electron Microscopy from micromagnetic simulations, *arXiv:1207.2310 [cond-mat]* (2012).
- [50] S. D. Pollard, J. A. Garlow, J. Yu, Z. Wang, Y. Zhu, and H. Yang, Observation of stable Néel skyrmions in cobalt/palladium multilayers with Lorentz transmission electron microscopy, *Nature Communications* **8**, 14761 (2017).
- [51] X. Yu, M. Mostovoy, Y. Tokunaga, W. Zhang, K. Kimoto, Y. Matsui, Y. Kaneko, N. Nagaosa, and Y. Tokura, Magnetic stripes and skyrmions with helicity reversals, *Proceedings of the National Academy of Sciences* **109**, 8856 (2012).
- [52] M.-A. Bisotti, D. Cortés-Ortuño, R. Pepper, W. Wang, M. Beg, T. Kluyver, and H. Fangohr, Fidimag – A Finite Difference Atomistic and Micromagnetic Simulation Package, *Journal of Open Research Software* **6**, 22 (2018).
- [53] P. F. Bessarab, V. M. Uzdin, and H. Jónsson, Method

- for finding mechanism and activation energy of magnetic transitions, applied to skyrmion and antivortex annihilation, *Computer Physics Communications* **196**, 335 (2015).
- [54] D. Cortés-Ortuño, W. Wang, M. Beg, R. A. Pepper, M.-A. Bisotti, R. Carey, M. Vousden, T. Kluyver, O. Hovorka, and H. Fangohr, Thermal stability and topological protection of skyrmions in nanotracks, *Scientific Reports* **7**, 4060 (2017).

# Supplementary Materials

## S1. MAGNETIC PROPERTIES OF MULTILAYER SAMPLES

The magnetic properties of the samples studied in this work are tabulated in Table S1 and plotted in Figure S1. The saturation magnetization,  $M_s$ , and effective anisotropy,  $K_{\text{eff}}$ , were determined from magnetometry measurements (see Figure S2a-d). Following procedures established in previous works<sup>4</sup>, the exchange stiffness,  $A_{\text{est}}$ , was estimated with density functional theory (DFT)<sup>29</sup>. Meanwhile, the iDMI value,  $D_{\text{est}}$  was estimated by comparing the periodicity of micromagnetic simulations at zero field with that from magnetic force microscopy (MFM) images (see Figure S2q-t)<sup>1,2,4</sup>. Notably, the values  $A_{\text{est}}$  and  $D_{\text{est}}$  for the 14x multilayers studied in this work are in good agreement with values obtained for corresponding 1x films from Brillouin light scattering (BLS) experiments<sup>29</sup>. To check if a small iDMI affects the simulation of the  $^{\text{S}}\text{Co}(10)$  stack, we performed additional hysteresis loop simulations with iDMI of 0.1 mJ/m<sup>29</sup> and found the results to be virtually identical to our original zero iDMI simulations.

In Figure S2, we show the magnetization hysteresis loops,  $M(H)$ , with applied field  $\mu_0 H$  in the in-plane (IP) and out-of-plane (OP) directions. We also show an overview of LTEM, MTXM and micromagnetic simulations for the four samples at zero field or low fields, in the labyrinthine stripe state. The magnetic morphology captured by the

Acronym	Stack Composition	$M_s$	$K_{\text{eff}}$	$D_{\text{est}}$	$A_{\text{est}}$	$\kappa$
		(MA/m)	(MJ/m <sup>3</sup> )	(mJ/m <sup>2</sup> )	(pJ/m)	
$^{\text{S}}\text{Co}(10)$	[Pt(10)/Co(10)/Pt(10)] <sub>14</sub>	1.18	0.68	0	17.3	0
<b>Fe(0)/Co(10)</b>	[Ir(10)/Co(10)/Pt(10)] <sub>14</sub>	0.88	0.47	1.3	17.8	0.3
<b>Fe(2)/Co(8)</b>	[Ir(10)/Fe(2)/Co(8)/Pt(10)] <sub>14</sub>	0.93	0.22	1.8	12.8	0.9
<b>Fe(3)/Co(7)</b>	[Ir(10)/Fe(3)/Co(7)/Pt(10)] <sub>14</sub>	0.96	0.08	2.0	13.6	1.5

Table S1. **Magnetic properties of multilayer samples.** List of multilayer samples used in this work, with layer thickness in angstroms in parentheses. The magnetic properties – saturation magnetization ( $M_s$ ), effective magnetic anisotropy ( $K_{\text{eff}}$ ), estimated iDMI ( $D_{\text{est}}$ ), estimated exchange stiffness ( $A_{\text{est}}$ ) as well as the stability parameter,  $\kappa$  – are tabulated.

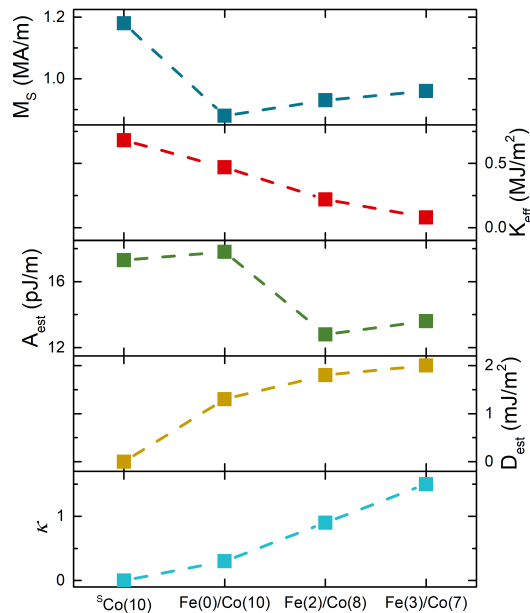


Figure S1. **Magnetic properties of multilayer samples.** The trendlines of  $M_s$ ,  $K_{\text{eff}}$ ,  $A_{\text{est}}$ ,  $D_{\text{est}}$  and  $\kappa$  across samples. The samples are arranged in order of increasing  $\kappa$ .



two experimental imaging techniques is consistent. The simulation results are also largely in agreement with the experimental images.

## S2. IMAGE ANALYSIS

The analysis of LTEM and MTXM images used in this work was performed with custom-written Python code. To remove low spatial frequency background, a duplicate convolved with a large Gaussian kernel was subtracted from the original image. To reduce the high spatial frequency noise while preserving as much information as possible, a small median filter was then applied. In cases where binarization was required, the threshold was automatically selected using the Otsu algorithm. To remove further noise, if any, small regions below a certain areal threshold were disregarded.

Manuscript Fig. 2 shows the averaged domain width from MTXM images. To obtain this result, background removal, denoising and binarization were performed as described above. Next, a Euclidean distance transform – which yields the shortest distance from the domain edge to the medial axis – was applied on the binarized image using built-in functions in the scikit-image library<sup>48</sup>. Finally, the average domain width was extracted as twice the average distance to the medial axis.

Manuscript Fig. 1 shows linecuts across stripe domains at fixed intervals from LTEM images. To obtain these linecuts, a skeletonization operation was enacted on the LTEM images after the basic image processing and binarization described above. Next, all foreground pixels connected to more than two other pixels were removed.

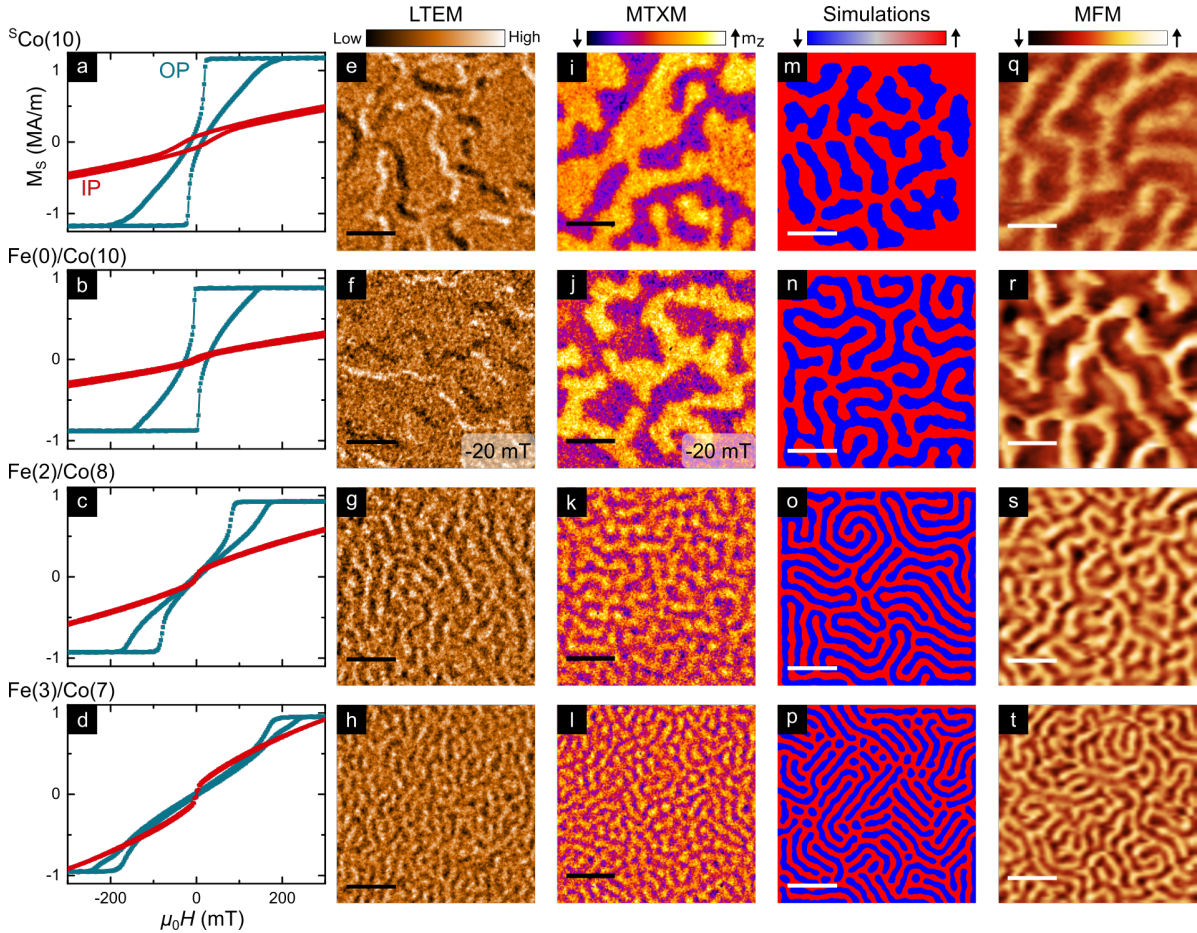


Figure S2. **Overview of magnetometry and magnetic imaging.** (a-d) Magnetization hysteresis loops for in-plane (IP, red) and out-of-plane (OP, teal) orientations of applied field,  $\mu_0 H$ , across all four samples. Equilibrium magnetic configurations of all four samples as observed in (e-h) LTEM images ( $\alpha = 20^\circ$  and  $-2$  mm defocus), (i-l) MTXM images, (m-p) micromagnetic simulations and (q-t) MFM images. All images are at the same scale and are acquired at zero-field apart than (f,j), which are at  $-20$  mT. Scalebar:  $0.5 \mu\text{m}$ .

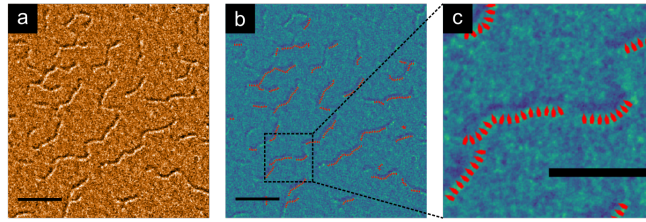


Figure S3. **Illustration of linecut analysis for LTEM images.** An illustration of the intermediate processing steps used to obtain linecuts from LTEM images shown in manuscript Fig. 1f-g. **(a)** Raw LTEM image of Fe(0)/Co(10) at  $-100$  mT,  $\alpha = -20^\circ$  and  $-2$  mm defocus (scalebar: 1  $\mu\text{m}$ ). **(b)** Algorithmically determined linecuts (red lines) overlaid on the image in (a). **(c)** A zoomed-in view of (b), showing individual linecuts, as indicated by arrows (scalebar: 0.5  $\mu\text{m}$ ).

This ensured that there were no branches and that all regions, defined as foreground pixels that are 4-connected, are linear. Each region was then fitted to a spline, and the normal to the spline was computed. Finally, linecuts were acquired from the original, unprocessed LTEM image using methods in scikit-image library, at regular intervals on the spline. Linecuts exceeding the boundaries of the image were excluded. The position and the direction of the algorithmically chosen linecuts are shown in Figure S3. The acquired linecuts were further binned by angle, and only those within  $10^\circ$  from the tilt axis were included in calculating the averaged output.

For analysis of LTEM images acquired at varying tilt angles, an additional preprocessing step was required. The sequence of images had to be aligned to the first image, as the latter was used to determine the position of each linecut. The image alignment was done manually with ImageJ by selecting about 15 corresponding landmarks on each image and calculating an affine transformation to map each image in the tilt sequence to the first image. Manuscript Fig. 1 does not show the linecut for zero tilt of Fe(0)/Co(10). This is because, in the absence of visible magnetic textures at zero tilt, the alignment landmarks for that image could not be located. Similar image sequence alignment issues precluded the use of this method for analyzing Fe(3)/Co(7) images (see § S3).

Manuscript Fig. 4 details the statistics of skyrmion and stripe number densities with varying magnetic field, which were obtained as follows. For micromagnetic simulations (manuscript Fig. 4c,d), algorithmic counting gave reliable results after denoising and binarization due to the high signal-to-noise ratio (SNR) of domains in simulated images. Domains that exceeded a visually determined circularity threshold of 0.65, were classified as skyrmions, while the remainder otherwise, were counted as stripes. Here, circularity is defined as  $4\pi A/P^2$ , where  $A$  and  $P$  are the area and perimeter of the domain respectively. For LTEM, attempts to use such algorithmic counting of stripes and skyrmions did not give results consistent with visual inspection. Hence, we visually identified every texture in LTEM images as a skyrmion or stripe. A typical LTEM image of Fe(2)/Co(8) with skyrmions and stripes identified as above is shown in Figure S4.

### S3. LTEM IMAGING

In this work, spatial evolution of LTEM contrast of textures has been used to quantify their helicity. As LTEM contrast is not intuitive to non-experts, we show in Figure S5 the simulated LTEM contrast – generated using an open-source software, MALTS<sup>49</sup> – for an idealized magnetic stripe with Bloch and Néel DWs. Also shown are the linecuts perpendicular to the domain for various tilt angles (c.f. manuscript Fig. 1f-g). At zero tilt, the Bloch DW pair produces contrast symmetric about the center of the stripe, whereas the Néel DW pair give zero contrast. In both cases, an additional antisymmetric contrast is present for finite tilt.

In manuscript Fig. 1, we have shown tilt-dependent LTEM data for  $^5\text{Co}(10)$ , confirming Bloch helicity of its DWs, and for Fe(0)/Co(10) – wherein DWs have Néel helicity. In Figure S6, we show for comparison LTEM data for Fe(2)/Co(8), which also has, unsurprisingly, Néel DWs. Finally, the linecut extraction technique used for the previous three samples could not be applied to Fe(3)/Co(7). In this case, owing to the higher texture density, images with varying tilt could not be reliably aligned (see § S2). Nonetheless, a visual inspection of the contrast evolution with tilt suggests that the textural helicity for Fe(3)/Co(7) is very similar to that of Fe(2)/Co(8) hosting Néel DWs.

The transport-of-intensity equation (TIE) has previously been used to reconstruct the magnetization of Bloch and Néel textures with varying degrees of success<sup>50</sup>. Correspondingly in Figure S7, we show the IP magnetic induction

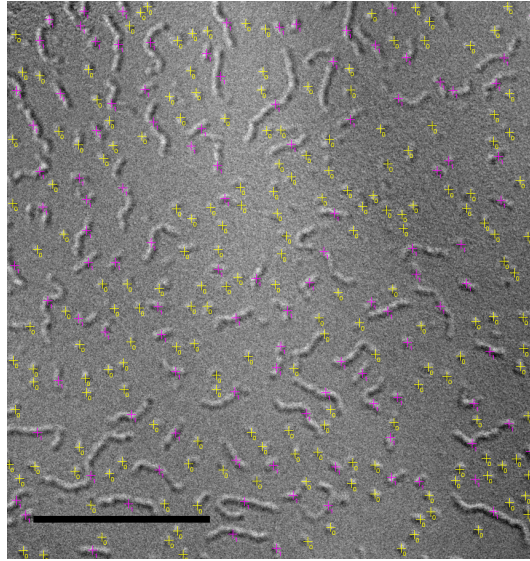


Figure S4. **Identification of textures in LTEM images.** A representative LTEM image of Fe(2)/Co(8) at 150 mT,  $\alpha = 20^\circ$  and  $-2$  mm defocus (scalebar: 1  $\mu$ m) used to demonstrate the counting of observed skyrmions and stripes. Skyrmions are indicated with yellow crosses, and stripes with pink crosses.

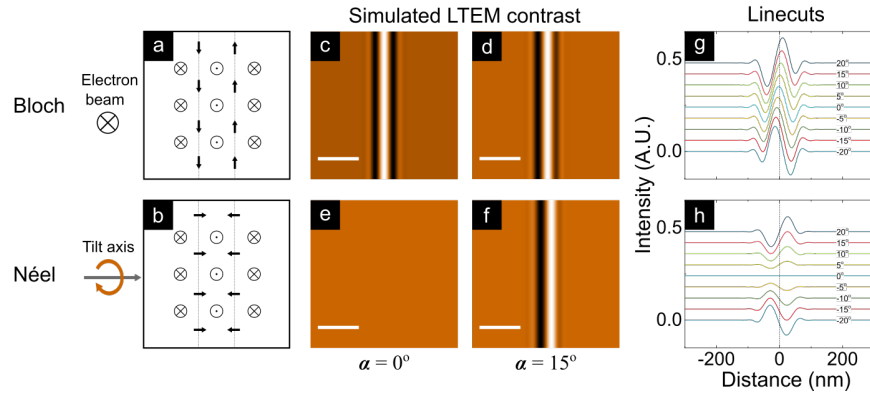


Figure S5. **Simulated LTEM contrast.** (a-b) Schematic of an artificially constructed magnetic stripe for MALTS simulations with Bloch and Néel DWs respectively. Vector symbols represent the direction of the electron beam and local magnetization. (c-f) MALTS simulated LTEM contrast at  $\alpha = 0^\circ$  and  $15^\circ$  (scalebar: 200 nm). (g-h) Linecuts across the simulated LTEM images with  $\alpha$  varying over  $\pm 20^\circ$ .

for  $^{\text{S}}\text{Co}(10)$  and Fe(0)/Co(10), each reconstructed using two LTEM images at defoci of  $\pm 2$  mm using a TIE-based commercial software, QPt<sup>TM</sup> for Digital Micrograph from HREM Research, Japan (c.f. manuscript Fig. 1). For  $^{\text{S}}\text{Co}(10)$ , we can clearly see the evidence for Bloch DWs in Figure S7c. In contrast, for Fe(0)/Co(10), due to the finite tilt angle, a part of the out-of-plane magnetization of the textures are projected in-plane and is visible in Figure S7d. Crucially, no evidence of Bloch DWs is detectable for Fe(0)/Co(10).

In manuscript Fig. 2, we present MTXM results as direct experimental evidence when investigating domain compressibility as a function of  $\kappa$ . The same trend could be observed indirectly with LTEM. To this end, LTEM imaging was performed along a hysteresis loop, as shown in Figure S8a-d. It is visually apparent that at low fields of  $-20$  mT, the average domain width is much greater for Fe(0)/Co(10) (Figure S8a) than that of Fe(2)/Co(8) (Figure S8c). However, at higher fields, their domain widths are comparable (Figure S8b,d). This visual observation could be placed on quantitative standing if we employ the previously established algorithmic linecut analysis, but this time as a function of the magnetic field, as shown in Figure S8e,f (c.f. MTXM in manuscript Fig. 2i). As the linecuts are centered on the intensity peaks, the domain width is simply the separation between the intensity peak (bright) and trough (dark) regions. For Fe(0)/Co(10) at low fields, the trough is separated  $\sim 200$  nm from the peak and is heavily smeared. This is because DWs are well separated (i.e. domains are wide) with weak spatial correlation. With increasing field, the trough moves towards the peak (i.e. domain width shrinks) and becomes



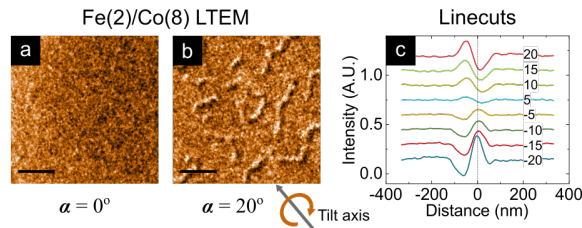


Figure S6. **LTEM analysis of DW helicity for Fe(2)/Co(8).** (a-b) LTEM images of Fe(2)/Co(8) sample at  $\alpha = 0^\circ$  and  $20^\circ$ , at a field of 100 mT and at  $-2$  mm defocus (scalebar:  $0.5 \mu\text{m}$ ). (c) Averaged cross-sectional linecuts determined over the experimental field-of-view with tilt angle varying over  $\pm 20^\circ$  (c.f. manuscript Fig. 1d-e).

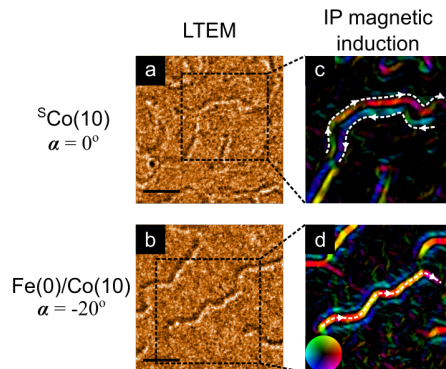


Figure S7. **Transport-of-intensity equation (TIE) analysis of LTEM images.** (a,b) LTEM images of  $^{\text{S}}\text{Co}(10)$  and  $\text{Fe}(0)/\text{Co}(10)$  at  $\alpha = 0^\circ$  and  $-20^\circ$  respectively (scalebar:  $0.5 \mu\text{m}$ ). (c,d) Reconstructed IP magnetic induction of  $^{\text{S}}\text{Co}(10)$  and  $\text{Fe}(0)/\text{Co}(10)$  using LTEM images acquired at defoci of  $\pm 2$  mm. The magnetization direction is represented by color. Inset to (d) shows color wheel, and white dotted lines with arrows are guides for the eye.

more correlated. This is consistent with the highly compressible behavior seen in MTXM data. In contrast, for  $\text{Fe}(2)/\text{Co}(8)$ , the peaks and troughs are always adjacent and have strong spatial correlation at all fields. This directly supports our claim that the domains are incompressible for  $\text{Fe}(2)/\text{Co}(8)$ .

#### S4. MICROMAGNETIC SIMULATIONS

Micromagnetic simulations were performed with MuMax3, using the magnetic parameters listed in Table S1<sup>47</sup>.

In the manuscript, we discuss the lack of evidence for hybrid chirality in  $\text{Fe}(0)/\text{Co}(10)$ ,  $\text{Fe}(2)/\text{Co}(8)$  and  $\text{Fe}(3)/\text{Co}(7)$  based on our LTEM data. Our micromagnetic simulations – which will be elaborated here – are consistent with our experiments in suggesting that hybrid chirality, if present at all, is very limited in these three samples.

The zero-field micromagnetic simulations were analyzed and DWs regions for each layer were isolated for analysis. Figure S9a-d shows the OP magnetization (grayscale) and IP orientation of the DW magnetization relative to the DW normal vector (colored ribbons). The dot and cross products of the magnetization unit vector with the normal unit vector of the DWs were computed, which can be identified as the degree of Néel and Bloch chiralities respectively. The averaged layer-dependent Néel and Bloch chiralities are plotted as a function of layer number for the four samples in Figure S9e-h.

Our simulations suggest that  $^{\text{S}}\text{Co}(10)$  ( $D_{\text{est}} = 0$ ) has considerable hybrid chirality<sup>19</sup>. The layers near the center have Bloch helicity, while the layers near the top and bottom form Néel caps, consistent with previous works<sup>19,27</sup>. However, upon considering all layers as a whole, both Bloch and Néel chiralities average to zero. Therefore, we label this sample as achiral<sup>39,51</sup>. In comparison, the other three samples –  $\text{Fe}(0)/\text{Co}(10)$ ,  $\text{Fe}(2)/\text{Co}(8)$  and  $\text{Fe}(3)/\text{Co}(7)$  – with  $D_{\text{est}} > 0$  are strongly chiral, i.e. have fixed handedness. Even if a Bloch center is present in  $\text{Fe}(0)/\text{Co}(10)$  ( $D_{\text{est}} = 1.3 \text{ mJ/m}^2$ ), it might only exist in one or two layers which is difficult to observe experimentally. Moreover, we show that  $\text{Fe}(0)/\text{Co}(10)$  is at the threshold of hybrid chirality since the Bloch center vanishes if we consider a

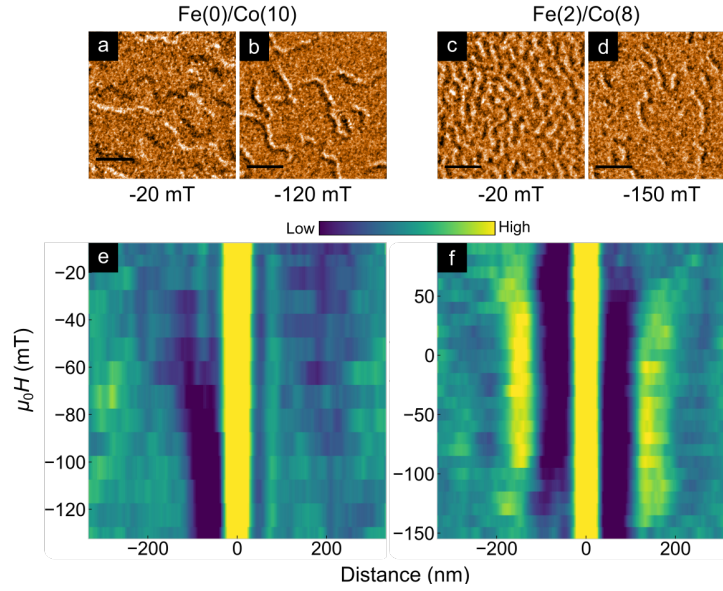


Figure S8. **Domain compressibility investigated by LTEM.** (a-d) Representative LTEM images of Fe(0)/Co(10) and Fe(2)/Co(8) at low and high magnetic fields (scalebar:  $0.5 \mu\text{m}$ ). (e,f) Stacked color plots of field-of-view averaged cross-sectional linecuts for Fe(0)/Co(10) and Fe(2)/Co(8) as a function of varying magnetic field (along y-axis). color represents LTEM intensity along the linecut.

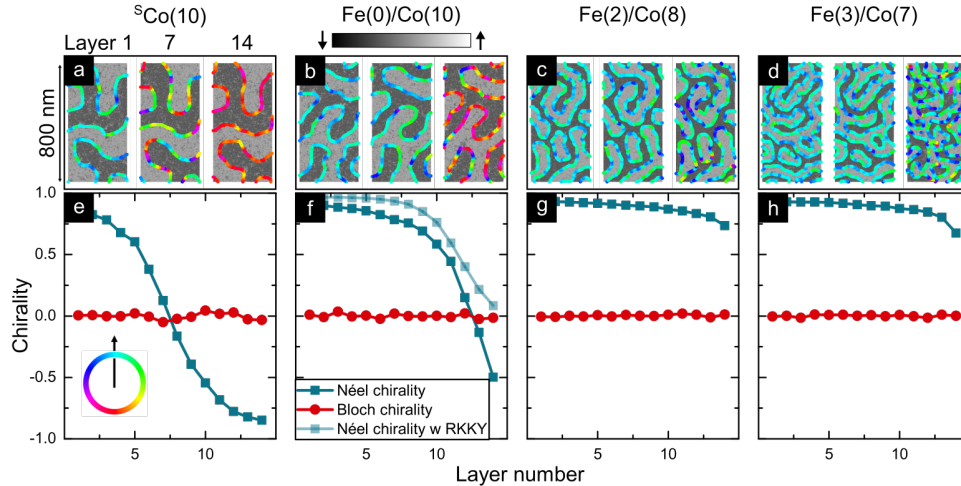


Figure S9. **Layer-dependent chirality of DWs from simulations.** (a-d) Representative cropped regions for layers 1, 7 and 14 from zero-field micromagnetic simulations of the four samples studied in this work. The grayscale colormap represents the OP magnetization, while colored ribbons show the IP magnetization orientation of the DWs relative to the DW normal vector. Inset in (e) shows the color wheel for IP orientation of DW magnetization, wherein the black arrow represents the direction of the DW normal. (e-h) The spatially averaged degree of Néel and Bloch chiralities as a function of layer number for the four samples. Here, the degree of Néel and Bloch chiralities are defined as  $\mathbf{n}_{\text{DW}} \cdot \mathbf{m}$  and  $\mathbf{n}_{\text{DW}} \times \mathbf{m}$  ( $\mathbf{n}_{\text{DW}}$  is the DW normal unit vector and  $\mathbf{m}$  is the magnetization unit vector) respectively. The light teal line plot in (f) shows Bloch chirality when interlayer RKKY coupling – at 20% of direct exchange – is considered.

small but finite interlayer RKKY coupling – amounting to 20% of  $A_{\text{est}}$  – as shown in Figure S9f<sup>43</sup>. Hence, within this work, our simulations demarcate the boundaries of hybrid chirality as  $\kappa \lesssim 0.3$ . Meanwhile, we do not expect a Bloch center in Fe(2)/Co(8) and Fe(3)/Co(7) ( $D_{\text{est}} \geq 1.8 \text{ mJ/m}^2$ ), since their Néel chirality did not change sign across layers.

Hysteresis loops are simulated by time-stepping in the presence of a sweeping applied magnetic field<sup>47</sup>. The rate of field sweep is approximately  $10^6 \text{ T/s}$  due to computational constraints, and so an entire hysteresis loop simulation is swept in about 600 ns. In order to ensure that simulated magnetization configurations may cross

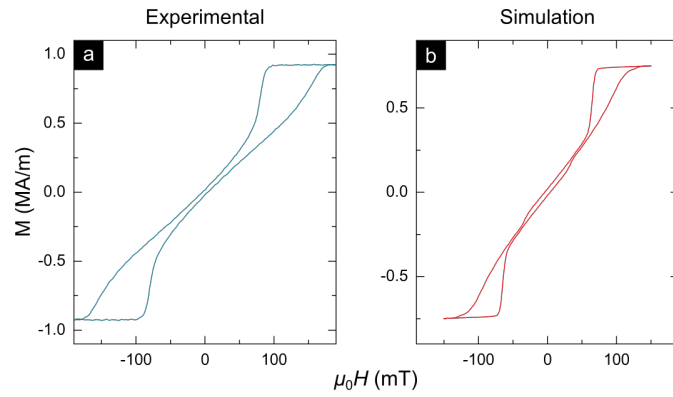


Figure S10. **Hysteresis loop simulation.** Comparison of the (a) experimental and (b) simulated OP hysteresis loop for sample Fe(2)/Co(8). Hysteresis loop simulations were performed with MuMax3 using procedures described in the text.

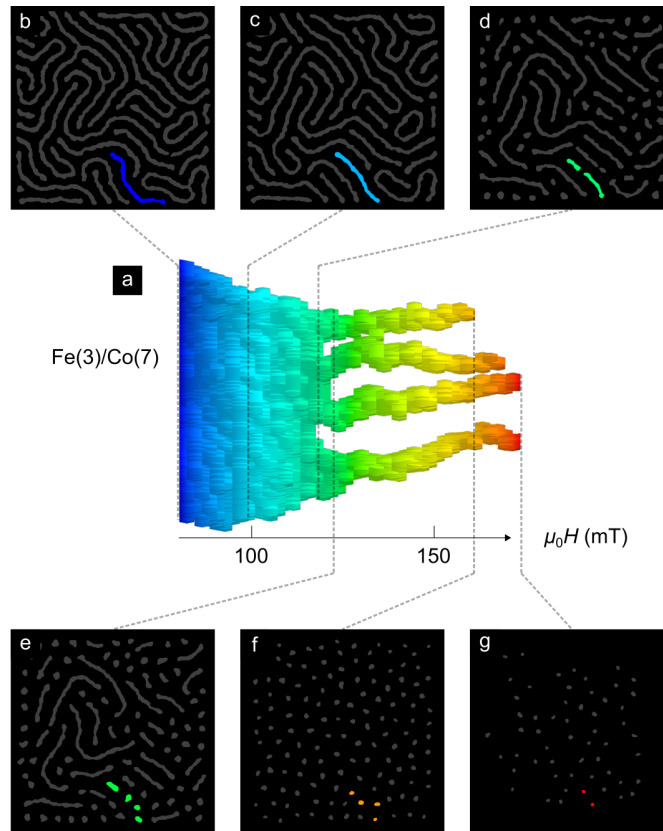


Figure S11. **Construction of a field evolution map of a typical domain.** (a) Field evolution map of a typical Fe(3)/Co(7) domain as shown in manuscript Figure 4b. Color denotes the magnitude of the magnetic field. (b-g) Simulated magnetization images (field-of-view:  $2 \mu\text{m}$ ) at various fields that are combined to construct (a). The chosen domain(s) is (are) highlighted in each slice.

energy barriers at rates corresponding to conventional magnetometry experiments despite these constraints, the simulation temperature needs to be correspondingly elevated (e.g. to 850 – 900 K). A typical hysteresis loop simulation result is shown in Figure S10 for direct comparison with experiments. Notwithstanding quantitative discrepancies of  $\sim 20\%$  in saturation field and magnetization, the simulated hysteresis loops fully reproduce the key experimental features, such as the sheared shape and various kinks.

It is convenient to visualize skyrmion formation from magnetic stripes in simulations with a “field evolution map” of a typical magnetic domain. This is created by stacking the 2D footprint of a typical domain across varying fields into a 3D object, where the third axis is the magnetic field. This process is illustrated in Figure S11, where the chosen domain is in color. This 3D object is then rotated such that the field axis is horizontal, as shown

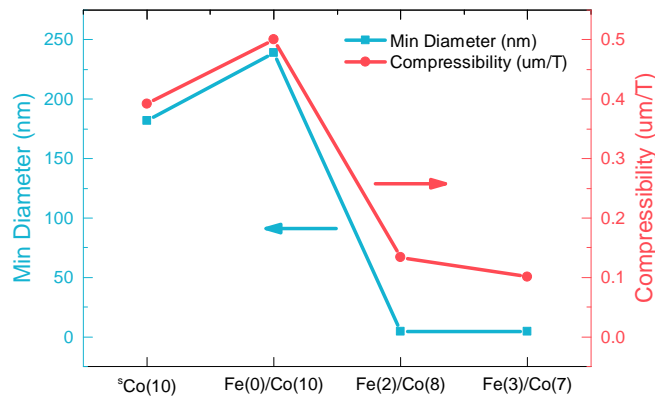


Figure S12. **Minimum skyrmion diameter predicted from isolated skyrmion model.** Theoretical results obtained by feeding in magnetic parameters listed Table S1 into model of isolated skyrmions<sup>21</sup>. This is compared with experimentally measured compressibility from manuscript Fig. 2k. The trends of both metrics are in close agreement – a sharp divide separates bubble skyrmions ( $^{55}\text{Co}(10)$ , Fe(0)/Co(10)) from compact skyrmions (Fe(2)/Co(8), Fe(3)/Co(7)).

in manuscript Fig. 4a,b. The mapping of the chosen domain across image slices in the magnetic field sweep is established using their spatial overlap – since the domains do not move appreciably within one field step.

We also include two supplementary videos showing the evolution of the magnetic textures as a function of applied field that is used in the construction of manuscript Fig. 4(a,b).

**Video 1:** This video shows the simulated evolution of magnetic textures of Fe(2)/Co(8) over a  $2\ \mu\text{m}$  field-of-view from 72 mT to 132 mT. Highlighted domains denote the representative evolution of stripes to skyrmions for Fe(2)/Co(8), and are horizontally stacked across fields to form manuscript Fig. 4(a).

**Video 2:** This video shows the simulated evolution of magnetic textures of Fe(3)/Co(7) over a  $2\ \mu\text{m}$  field-of-view from 80 mT to 170 mT. Highlighted domains denote the representative evolution of stripes to skyrmions for Fe(3)/Co(7), and are horizontally stacked across fields to form manuscript Fig. 4(b).

## S5. GEODESIC NUDGED ELASTIC BAND (GNEB) SIMULATIONS

GNEB atomistic calculations were performed with the Fidimag package<sup>52</sup>. A single layer of magnetic spins arranged in a two-dimensional square lattice with a cell size of  $1\ \text{nm} \times 1\ \text{nm}$  was used for all the GNEB simulations.

GNEB is a well-established method to calculate the energy barrier for a transition between two fixed metastable magnetic configurations, under the constraint of fixed magnetic moments magnitude<sup>53</sup>. Since GNEB is an atomistic calculation, the energies of the configurations are calculated in accordance with the atomistic Heisenberg Hamiltonian, taking into account exchange, DMI, uniaxial anisotropy and magnetostatic interactions<sup>54</sup>. To estimate the energy barriers of the stripe-skyrmion fission process, the initial metastable configuration was chosen to be single stripe domain relaxed at  $-0.04\ \text{mT}$ , and the final configuration to be two metastable skyrmions relaxed at the same external field. A total of 16 intermediate transition states and their energies were calculated by the GNEB algorithm, from which the energy barrier of the process can be estimated by interpolation. The resulting energy barriers of the stripe-skyrmion transition for Fe(2)/Co(8) and Fe(3)/Co(7) are shown in the main text.

## S6. COMPRESSIBILITY

Here, we compare two metrics that can be used to differentiate bubble skyrmions and compact skyrmions. In Figure S12, we show the compressibility of stripes reproduced from manuscript Fig. 2k and minimum diameter of isolated skyrmions<sup>21</sup> for the four samples in this work. Both metrics show a clear distinction between  $^{55}\text{Co}(10)$ , Fe(0)/Co(10) (bubble skyrmions) and Fe(2)/Co(8), Fe(3)/Co(7) (compact skyrmions).

One might notice a correlation between domain compressibility,  $\langle dW/dH \rangle$  and  $K_{\text{eff}}$ . We believe that this correlation arises from the fact that  $\kappa = \pi D/4\sqrt{AK_{\text{eff}}}$ , and therefore  $K_{\text{eff}}$  is a component of  $\kappa$ . Here, we show with micromagnetic simulations that  $K_{\text{eff}}$  cannot fully account for the domain compressibility trends. We study a fictitious sample, labeled as Fe(2)/Co(8)+, which has identical magnetic parameters as Fe(2)/Co(8) — including  $K_{\text{eff}}$

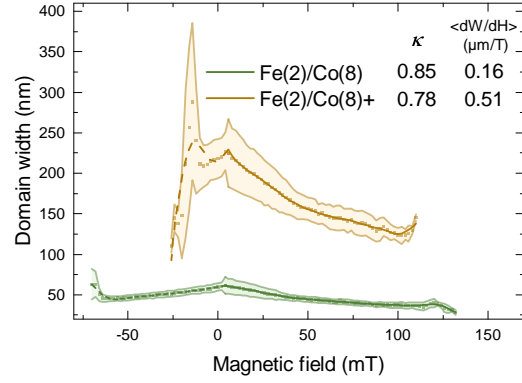


Figure S13. **Simulated domain width field evolution of Fe(2)/Co(8) and Fe(2)/Co(8)+.** Micromagnetic simulations of domain width as functions of applied magnetic field of Fe(2)/Co(8) and Fe(2)/Co(8)+, a fictitious sample with identical magnetic parameters as Fe(2)/Co(8) except an exchange stiffness that is 20% larger than Fe(2)/Co(8). Inset lists the  $\kappa$  and  $\langle dW/dH \rangle$  values for both samples.

– except a direct exchange,  $A_{\text{est}}$ , that is 20% larger, which results in a smaller  $\kappa$ . We simulate the hysteresis loop of Fe(2)/Co(8)+, extract the domain width and compute the  $\langle dW/dH \rangle$  using the same protocol as detailed in the manuscript. The comparison between Fe(2)/Co(8) and Fe(2)/Co(8)+ is shown in Figure S13. As can be seen,  $\langle dW/dH \rangle$  can vary considerably even if  $K_{\text{eff}}$  is kept constant across samples.

---